Journal of Alloys and Compounds 830 (2020) 154532

Contents lists available at ScienceDirect

Journal of Alloys and Compounds

journal homepage: http://www.elsevier.com/locate/jalcom

Effect of carbide formation on phase equilibria and compositional modulation of transformation properties in $(Mn,Fe)_2(P,Si)$ alloys

T.D. Brown [a], D. Galvan [a], J. van Buskirk [a], A. Mott [b], P.J. Shamberger [a, *]

[a] 575 Ross St. # 248, Department of Materials Science and Engineering, Texas A&M University, College Station, TX, 77840, USA
[b] 1617 Research Parkway, Frederick E. Giesecke Engineering Research Building, Texas A&M University, College Station, TX, 77845, USA

ARTICLE INFO

Article history:
Received 31 July 2019
Received in revised form
13 February 2020
Accepted 25 February 2020
Available online 26 February 2020

Keywords:
Magnetocaloric
Phase transitions
Phase diagrams
Microstructure
Transition metal alloys and compounds
Carbide formation
Solid state reactions
Powder metallurgy

ABSTRACT

Practical implementation of efficient magnetocaloric effect-based refrigeration and energy conversion applications requires the design of whole alloy families with narrow tolerances on the transformation properties, and therefore composition, of the component alloys. In the promising class of magnetocaloric $(Mn,Fe)_2(P,Si)$ alloys, this task of compositional tuning is made especially difficult by the observed co-existence of several P-depleted impurity phases, which for example, increases both the P content and transformation hysteresis losses of the main quaternary phase. In this work, we study the mechanisms that induce impurity phase formation in the Mn–Fe–P–Si system, and investigate the impact of sequential carbide formation on observed phase microstructure along with its effect on the composition and transformation properties of the $(Mn,Fe)_2(P,Si)$ phase. Using quantitative analyses to measure the composition within main and impurity phases in samples throughout the bulk alloy space, we establish that (1) repeated processing steps increase the content of a $(Mn,Fe)_9Si_2$ carbide phase, resulting in (2) deviations in the magnetocaloric $(Mn,Fe)_2(P,Si)$ phase from bulk nominal composition of up to ~4 at. %. Finally, we map out (3) the dependence of transformation critical temperature, hysteresis, and enthalpy on the composition of the $(Mn,Fe)_2(P,Si)$ phase of interest. Together, these results suggest carbon impurities can have a critical impact on magnetocaloric transformation properties in $(Mn,Fe)_2(P,Si)$ alloys, since 0.3 wt % carbon content can cause critical temperatures and hystereses to deviate by more than 95 K and 8 K from desired design values.

1. Introduction

Magnetocaloric alloy systems like $La(Fe,Si)_{13}$, Ni–Mn-X metamagnetic shape memory alloys, and $(Mn,Fe)_2(P,Si)$ manifest coupled first-order magneto-structural transformations (MSTs) [1–4], making them of primary interest for room temperature solid-state magnetic refrigeration [5–7] and thermomagnetic generation applications [8,9]. In order to most efficiently inter-convert thermal and magnetic energy in these applications, systems must be designed with large heat absorption and minimal losses distributed across large temperature ranges, for example, with graded regenerator beds [10]. At the materials level, this translates directly into designing families of magnetocaloric alloys whose MSTs all generate maximum entropy of transformation and minimal hysteresis loss, each with some different critical temperature near room temperature. While compositional tuning offers a practical means to control all of these MST properties [11–13], they tend to be strongly correlated, and so independent control is possible only along a handful of paths in composition space. Hence, controllably designing magnetocaloric alloy compositions within narrow tolerances is absolutely critical to further development for refrigeration and generation applications.

Compounding the problem, magnetocaloric alloys are multi-component systems, and the phase of interest manifesting MST often has a limited region of solid solubility. This results in phase segregation under certain processing conditions, and therefore less content of the MST phase and dilution of its effective transformation entropy/enthalpy, as well as substantial deviation of the MST phase from the designed bulk nominal composition. This phenomenon and its effects on transformation properties are already well-studied in the La–Fe–Si and Ni–Mn-X Heusler magnetocaloric systems. In the former, emergence of Fe-rich α–(Fe,Si)

* Corresponding author.
E-mail addresses: tdbrown0323@tamu.edu (T.D. Brown), dgalvan2148@tamu.edu (D. Galvan), jvanbuskirk0@tamu.edu (J. van Buskirk), andrew.v.mott@tamu.edu (A. Mott), patrick.shamberger@tamu.edu (P.J. Shamberger).

https://doi.org/10.1016/j.jallcom.2020.154532
0925-8388/

and La-rich $La_1Fe_1Si_1$ phases induces a Si-rich La(Fe,Si)$_{13}$ phase with suppressed MST critical temperature [14–17]; in the latter, a similar Co-rich γ disordered FCC phase [18,19] induces an In-poor (Ni,Co)$_2$(Mn,In) phase with increased critical temperature [20] and broadened transformation width [21,22]. Subsequent work has investigated the phase equilibria and formation kinetics of these impurity phases, leading directly to the suppression of these phases through new processing techniques. Thus, clarification of the peritectic/peritectoid $\alpha + La_1Fe_1Si_1 \rightarrow La(Fe,Si)_{13}$ reaction [23–27] has produced novel melt-spinning and vacuum suction casting [28,29], and rapid quench/ball milled [30] processes that effectively seed the as-cast alloys with many small La(Fe,Si)$_{13}$ nuclei. These small nuclei rapidly grow during annealing, with substantial reductions in post-annnealing time required to yield a majority La(Fe,Si)$_{13}$-phase microstructure [31,32]. In contrast, the $L \rightarrow \gamma + L2_1$ eutectic reaction [33,34] in NiCoMnIn can be suppressed through rapidly-quenched melt-spinning processing.

In the present Mn–Fe–P–Si alloy system, the quaternary composition provides one extra degree of freedom, enabling nearly independent tuning of MST transformation temperature and hysteresis [35,36], as required for systematic design of a regenerator bed. However, this advantage is practically negated by impurity phase formation, with P-depleted (Mn,Fe)$_3$Si and (Mn,Fe)$_5$Si$_3$ phases [37–39] thought to create a P excess in the transforming (Mn,Fe)$_2$(P,Si) phase [40], thereby lowering its critical temperature and increasing its hysteresis [41–43]. Although it is suggested that higher Fe content can suppress the (Mn,Fe)$_3$Si phase [44] and element additions like B can help stabilize the (Mn,Fe)$_2$(P,Si) phase [45,46], these create their own effects on transformation temperature and hysteresis, again complicating systematic alloy design. Microstructural studies suggest that neither peritectic or eutectic reaction paths described above are relevant to this system: the former being excluded by the immediate formation of (Mn,Fe)$_2$(P,Si) phase post-casting and its continuous growth on subsequent annealing without peritectic phase competition [47]; the latter by the segregation of impurity phases at (Mn,Fe)$_2$(P,Si) grain boundaries, as opposed to eutectic fine lamellae [48]. Finally, recent work has explored the role of carbon doping on the unit cell expansion and subsequent transformation properties of the alloy composition $Mn_{1.15}Fe_{0.80}P_{0.50}Si_{0.50}$-C [49], but further investigation is needed to relate these to the presence and composition of the impurity phases. Hence we are motivated to study quantitatively how the emergence of impurity phases affects the (Mn,Fe)$_2$(P,Si) phase's transformation properties and likely mechanisms by which these impurities form, so that their effect on magnetocaloric transformation properties can be suppressed.

In this work, we further investigate the mechanisms behind the phase segregation leading to compositional modulation in $(Mn_xFe_{2-x})(P_{1-y}Si_y)$ alloys and their impact on the resulting magneto-structural transformation properties. Through quantitative compositional analyses of transforming quaternary and non-transforming P-depleted phases in alloys throughout the composition space, we establish that (1) carbon addition plays a critical role in the emergence of impurity phases, with the content of at least one P-depleted carbide phase increasing steadily from 1 vol % to 7 vol % after repeated processing cycles and (2) the presence of these P-depleted carbides further affects the composition of the transforming phase of interest, resulting in deviations of up to 4 at. % Si or P and 2 at. % Mn or Fe from desired bulk nominal compositions. Finally, we (3) quantify the underlying sensitivity of transformation critical temperature, hysteresis, and enthalpy on composition of the transforming (Mn,Fe)$_2$(P,Si) phase, showing for example that a deviation of 1 at. % Si can modulate transformation critical temperatures and hysteresis by as much as 26 K and 3 K, respectively. Together, these results suggest the importance of carbon-free processing to controllable synthesis of $(Mn_xFe_{2-x})(P_{1-y}Si_y)$ alloys for magnetocaloric applications, since relatively minor amounts of 0.3 wt % volume-averaged carbon content can cause transformation critical temperatures and hystereses to deviate by more than 100 K and 15 K from desired design values.

2. Experimental methods

$(Mn_xFe_{2-x})(P_{1-y}Si_y)$ alloys with bulk alloy compositions $(1.18 \leq x \leq 1.28)$ and $(0.53 \leq y \leq 0.61)$ were synthesized by powder metallurgy starting from mixing about 10 g of 99.9% purity Mn and 99.99% Si powders [ESPI Metals, metals basis] with 99.5% Fe_2P and 99.99% red P powders [Sigma Aldrich] and high-energy milling in ZrO_2 milling jars with 3 mm ZrO_2 media [Retsch] at 250–300 rpm for 8 h. Milled powders were pressed under 1000 psi uniaxial stress into 8 mm diameter pellets and sealed into quartz ampoules with an oxy-methane torch. Pellets were subsequently sintered at 1373 K for 6 h followed by annealing at 1173 K for 20 h and furnace cooling to room temperature. Annealed pellets were re-ground and pressed into new pellets and re-cycled through the identical 1373 K/6 h + 1173 K/20 h heat treatment, with the samples directly after the first and second processing cycles designated "A" and "B", respectively, as in the remainder of the text. In all cases, care was taken to exclude non-metal contaminants from processing steps by mixing stock powders and pressing green pellets under glovebox Ar atmosphere (<0.1 ppm O_2, <0.5 ppm H_2O) and milling under Ar in milling jars sealed by vacuum grease and parafilm. A method was also developed to backfill quartz ampoules under glovebox atmosphere before melt sealing within 3–5 min, so that samples were never directly exposed to ambient atmosphere even briefly while in transit to be melt-sealed.

Electron micrographs and quantitative composition analyses *via* energy and wavelength dispersive spectroscopy (EDS and WDS) were taken using the Cameca SXFive electron microprobe. Quantitative composition analyses were computed from WDS scattering intensities using the MAC30 absorption correction tables. Phase compositions were measured by average spot (point) analyses using a beam voltage of 15 kV and a beam current of 20 nA with counting times of 20 s on peak and 10 s on each background. GaP was used as the P standard, while pure element standards were used for Mn, Fe, and Si. Carbon content was taken from carbon-by-difference measurements with respect to WDS scattering totals. Mean compositions and standard deviations were taken from twelve 5 μm spots in the majority (Mn,Fe)$_2$(P,Si) phase and three 1 μm spots in all other phases. Phase transformation properties of the processed alloys were characterized *via* differential scanning calorimetry (DSC) with a QA-20 system equipped with an RCS90 cooling unit [Thermal Analysis] at a standard 10 K/min ramp rate. First-order transformation critical temperatures and hystereses have been computed from DSC traces as the average and difference, respectively, of the peak temperatures on heating and cooling. Transformation enthalpies have been computed as the area between each heating/cooling peak and a sigmoidal baseline defined at four points where the derivative heat flow signal is approximately constant.

3. Results

3.1. Multiphase microstructure and measured phase compositions

After heat treatment, alloys throughout the composition space manifest a typical multiphase microstructure consisting of majority quaternary (Mn,Fe)$_2$(P,Si) phase with minor impurities on the order of 5–20 μm (Fig. 1). Qualitative composition mapping *via* Energy Dispersive Spectroscopy (EDS) confirms that the impurity phases

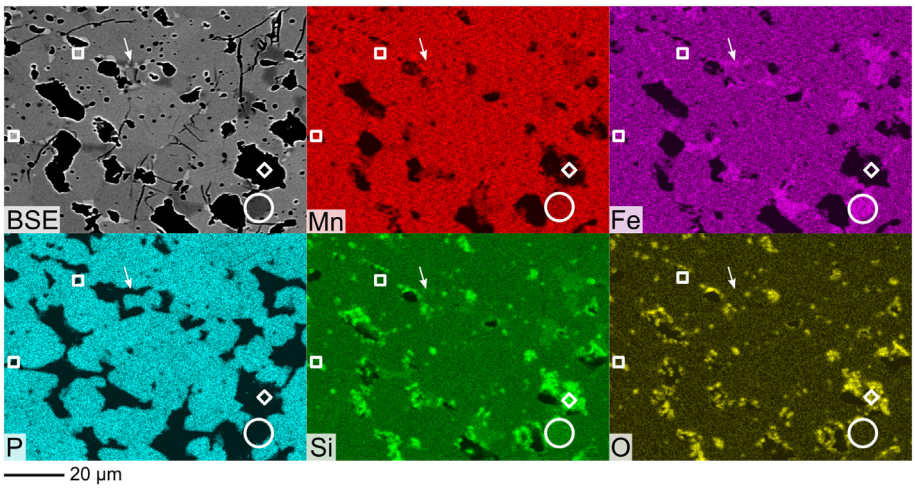

Fig. 1. Backscatter electron (BSE) image and corresponding Energy Dispersive Spectroscopy (EDS) elemental Mn, Fe, P, Si, O composition maps for $(Mn_xFe_{2-x})(P_{1-y}Si_y)$ alloy with bulk nominal ($x = 1.239$, $y = 0.559$) composition. Presence of P-depleted $(Mn,Fe)_9Si_2$ (white squares) and $(Mn,Fe)_5Si_2$ (white circles) phases and SiO_2 (white diamonds) causes composition of majority $(Mn,Fe)_2(P,Si)$ phase to deviate from the nominal composition.

are not merely P-poor, but essentially P-depleted, consistent with previous observations [40,41,44]. Although the impurity phases are most commonly observed as separate islands, they are occasionally observed within the same island (white arrow), which may indicate some close relationship between the phases in terms of their stability or when they form during the heat treatment process. Finally, much of the SiO_2 content appears as a thin coating within the voids, so that the volume fraction is likely substantially less than suggested by the relative area fraction in the backscatter and EDS images.

Further quantitative composition analysis *via* wavelength dispersive spectroscopy (WDS) confirms these initial observations (Table 1), and demonstrates substantial deviation in P and Si content in the $(Mn,Fe)_2(P,Si)$ phase from the nominal bulk composition. The P-depleted impurities observed in this particular sample evidently are not the $(Mn,Fe)_3Si$ and $(Mn,Fe)_5Si_3$ stoichiometries normally reported. However, the observed stoichiometries $z = 4.51$ and $z = 2.47$ are consistent with $(Mn,Fe)_9Si_2$ and $(Mn,Fe)_5Si_2$ phases, respectively, both of whose binary analogues Mn_9Si_2 and Mn_5Si_2 are found to be stable below 1150 K in the Mn–Si binary phase diagram [50–52]. Similar composition data have been recorded for the $(Mn,Fe)_2(P,Si)$ main phase and all observed P-depleted impurities throughout the $(Mn_xFe_{2-x})(P_{1-y}Si_y)$ composition space ($1.18 \leq x \leq 1.28$) and ($0.53 \leq y \leq 0.61$) (Fig. 2a), showing that the observed $(Mn,Fe)_9Si_2$ and $(Mn,Fe)_5Si_2$ phases, as well as the previously reported $(Mn,Fe)_3Si$ and $(Mn,Fe)_5Si_3$ phases, are all observed repeatedly throughout the alloy space. All four phases' binary analogues are found within the Mn–Si alloy system, suggesting that the multiphase microstructure observed in all of the alloys is tied to the intrinsic thermodynamic stability of the phases.

At the same time, carbon-by-difference analyses (see Supplementary Information) of the phase assemblages (Fig. 2b) show that out of all of the four observed impurity phases and the main $(Mn,Fe)_2(P,Si)$ phase of interest, only the $(Mn,Fe)_9Si_2$ has substantial >3 wt % C content, with all other phases' C content near the 0.3–0.5 wt % uncertainty level of the instrument. Hence, the P-depleted $(Mn,Fe)_9Si_2$ is actually a carbide phase, with a well-defined stoichiometry of (Mn,Fe):Si:C = 6:1:1, which we note is close to the Mn_5SiC phase predicted [53] and observed [54,55] in the Mn–Si–C ternary phase diagram near 1200 °C; we might expect a similar phase to be present in the quaternary system closer to 1000–1100 °C. The $(Mn,Fe)_2(P,Si)$ phase in particular is essentially carbon-free. Hence, although some amount of carbon is present in the alloys, it is incorporated within the phase of interest only at extremely low levels near the detection limit. However, this provides a clue that carbon may be indirectly influencing the phase of interest through the phase field mechanism above by somehow modifying the thermodynamic equilibrium of the P-depleted impurity phases, as observed in the multiphase microstructure.

3.2. Phase evolution during multiple annealing steps

In an attempt to allow potential long-range compositional gradients to relax and thereby drive the system towards thermodynamic equilibrium, each of the initially processed alloys were re-ground and pressed into new pellets under Ar before re-sintering and annealing in quartz ampoules under the same 1373 K/6 h + 1173 K/20 h heat treatment. The initial multiphase alloys after the first sintering-annealing step were designated "A", and those obtained after the second annealing step were designated "B." In fact, no additional homogenization effects from repeated

Table 1
Summary of compositions and metal-to-non metal ratio $z = (Mn + Fe) : (P + Si)$ of phases in Fig. 1 measured from spot-averaged wavelength dispersive spectroscopy (WDS) across the alloy surface. Means and standard deviations taken from twelve 5 μm spots in the majority $(Mn,Fe)_2(P,Si)$ phase and three 1 μm spots in the impurity phases. *Nominal bulk 99% CIs computed with measured weight accuracies of 1 mg are less than 10^{-3} at. %.

Phase	Mn/at. %	Fe/at. %	P/at. %	Si/at. %	(Mn,Fe)z(P,Si)
Nominal Bulk	41.3 ± 0.0*	25.4 ± 0.0*	14.7 ± 0.0*	18.6 ± 0.0*	2.00 ± 0.00
$(Mn,Fe)_2(P,Si)$	42.1 ± 0.2	25.0 ± 0.1	16.2 ± 0.3	16.7 ± 0.3	2.03 ± 0.01
$(Mn,Fe)_9(P,Si)_2$	47.1 ± 0.4	24.8 ± 0.1	0.3 ± 0.1	15.6 ± 0.1	4.51 ± 0.01
$(Mn,Fe)_5(P,Si)_2$	39.0 ± 0.1	32.1 ± 0.1	1.6 ± 0.1	27.2 ± 0.1	2.47 ± 0.02

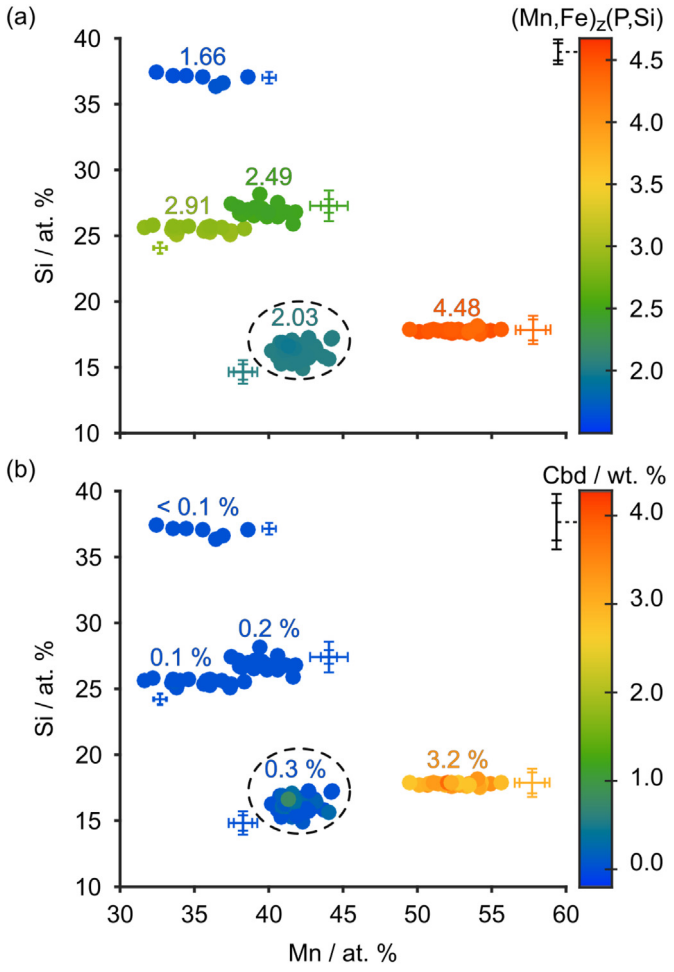

Fig. 2. Measured compositions of multi-phase assemblages across all samples taken from spot-averaged wavelength dispersive spectroscopy (WDS) in terms of Mn and Si contents, as well as (a) phase stoichiometry z, and (b) carbon-by-difference (Cbd) content. Characteristic error bars (1st and 3rd quartiles of measured uncertainties) for z and C for all samples, and for Mn/Si content for each distinct phase, are offset for visibility. Dashed circle identifies all measured $(Mn,Fe)_2(P,Si)$ phases of interest with $z \approx 2$ and $C \approx 0$.

processing were observed, and instead all "A" and "B" samples manifested from one to three of the P-depleted impurity phases. In many cases, the same impurities in an "A" sample persisted into its corresponding "B" sample, although occasionally one phase was observed to replace another in the "B" sample, strongly suggesting a conversion of one impurity into another. However, the annealing steps did affect the composition of the $(Mn,Fe)_2(P,Si)$ phase of interest, with the deviation of the "A" sample with respect to bulk nominal composition induced in the first annealing step being much larger than that of the "B" sample with respect to the "A" sample during the second step (Fig. 3). Even accounting for large inherent relative uncertainty due to taking the difference of nearly equal entities, the composition deviations induced during the first versus second step form non-overlapping populations, and the L_2 norm $\left|\left|\Delta\right|\right|_2 = \sqrt{\Delta \cdot \Delta}$ of the average deviation vector $\Delta := (\Delta Mn, \Delta Fe, \Delta P, \Delta Si)$ decreases substantially from 3.8 ± 0.8 at. % to 0.8 ± 0.5 at. % after repeated processing. The deviation produced in "A" samples during the first annealing step is large, especially considering, for example, the change in critical temperature with Mn in $(Mn_xFe_{2-x})(P_{0.4}Si_{0.6})$ is reported at -7.2 K/at. % [44].

Even after a repeated sequence of four processing steps yielding

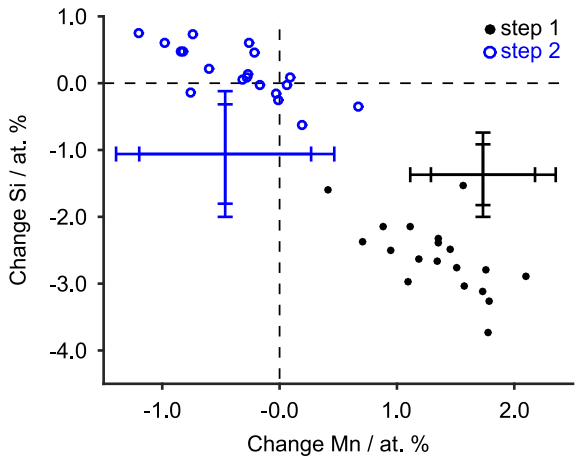

Fig. 3. Measured composition deviations of transforming quaternary phase of interest for all alloys between first "A" processing cycle with respect to bulk nominal (black, filled) and second "B" processing cycle with respect to composition after initial "A" processing (blue, unfilled). Characteristic error bars from first and third quartile of measured uncertainties for each group are shown offset for visibility. (For interpretation of the references to colour in this figure legend, the reader is referred to the Web version of this article.)

"A"-"D" type samples on the alloy with nominal composition ($x = 1.250$, $y = 0.640$), the multiphase structure is always observed (Fig. 4), including the $(Mn,Fe)_9Si_2$ carbide phase. The sequence of compositional deviation L_2 norms relative to each previous cycle of the $(Mn,Fe)_2(P,Si)$ phase again rapidly decreases from 3.3 ± 0.3 at. % to 0.9 ± 0.5, then remains about constant, changing slightly to 0.8 ± 0.2, then 1.2 ± 0.3 at. %, after the last two processing cycles (Table 2). However, despite multiple grinding and annealing cycles, the composition of the phase of interest shows no tendency to approach the nominal bulk composition, and we conclude that the observed multi-phase structure is likely due to the system existing at thermodynamic equilibrium in a multi-phase field, as opposed to a diffusionally-limited slow approach to an actual single-phase equilibrium.

4. Discussion

4.1. Effect of processing cycles on phase microstructure

While the persistence of multiphase microstructures throughout multiple re-grind and annealing steps is consistent with equilibrium in a multi-phase field, the continual shift of $(Mn,Fe)_2(P,Si)$ phase composition without tendency to approach the nominal bulk is unexpected. However, stability in the composition of the phases of interest is expected only if the relative content of each of the phases itself unchanges from cycle to cycle, and although we might expect this to be true for the carbon-free phases and the $(Mn,Fe)_2(P,Si)$ phase of interest, it is possible the amount of carbide phase may be changing. To prove that this is the case, we return to a quantitative analysis of the ($x = 1.250$, $y = 0.540$) "A"-"D" sample suite. For each sample, five thresholded 300 μm BSE micrographs have been collected, and volume fractions for each of the $(Mn,Fe)_2(P,Si)$ phase and the two $(Mn,Fe)_5Si_2$ and $(Mn,Fe)_9Si_2$ phases have been computed as normalized area fractions, after subtracting out the observed 21 ± 3 vol % of voids (Fig. 5a).

The computed volume fractions of the $(Mn,Fe)_9Si_2$ carbide phase clearly increase throughout from sample "A"-"D"; whereas the volume fraction of the non-carbonized $(Mn,Fe)_5Si_2$ phase increases or decreases only slightly in each step. Furthermore, because the

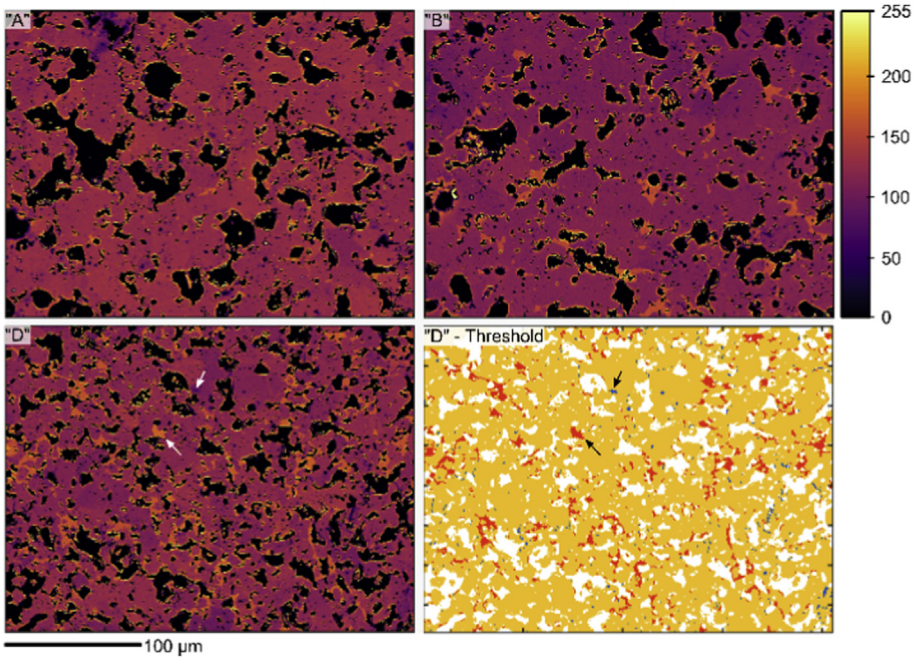

Fig. 4. Phase microstructure development of $(Mn_xFe_{2-x})(P_{1-y}Si_y)$ alloy with nominal ($x = 1.250$, $y = 0.540$) composition after repeated processing cycles "A"-"D". BSE intensity thresholding for "D" micrograph (lower right) emphasizes volume fractions of main $(Mn,Fe)_2(P,Si)$ phase (yellow), as well as impurity $(Mn,Fe)_5Si_2$ (blue) and $(Mn,Fe)_9Si_2$–C (orange). (For interpretation of the references to colour in this figure legend, the reader is referred to the Web version of this article.)

Table 2
Elemental composition deviations from nominal in sequentially carbonized alloys. The L_2 norm of the deviation vector, $\sqrt{(\Delta Mn)^2 + (\Delta Fe)^2 + (\Delta P)^2 + (\Delta Si)^2}$ is plotted in Fig. 5b.

Processing Cycle	ΔMn/at. %	ΔFe/at. %	ΔP/at. %	ΔSi/at. %	L2 Dev.
"A" vs. nom.	0.7 ± 0.2	−0.4 ± 0.1	2.1 ± 0.3	−2.4 ± 0.3	3.3 ± 0.3
"B" vs. nom	0.5 ± 0.2	−0.1 ± 0.1	1.5 ± 0.5	−1.9 ± 0.5	2.5 ± 0.5
"C" vs. nom	−0.1 ± 0.2	0.4 ± 0.2	1.5 ± 0.3	−1.8 ± 0.3	2.4 ± 0.3
"D" vs. nom	0.2 ± 0.2	0.1 ± 0.1	2.3 ± 0.3	−2.6 ± 0.3	3.5 ± 0.3

carbon content of the $(Mn,Fe)_9Si_2$ phase is about constant at 3.1 ± 0.1 wt % throughout, the total evident carbon content of the whole microstructure increases with each processing step (Fig. 5b). Hence, additional processing steps, which would otherwise homogenize the system and stabilize the phase compositions, actually form additional carbide phase. Either there is some small amount of impurity carbon in the starting materials that gradually precipitates as the system is brought up repeatedly to 1173 K–1373 K, or else some process in each sequential processing cyle is introducing a small random amount of carbon to the system (see Supplementary Information). At the same time, the composition of the $(Mn,Fe)_2(P,Si)$ phase is also affected by the sequential carbide-stabilizing steps, with a large deviation in its composition relative to the bulk nominal during the first step, followed by much smaller cycle-to-cycle changes after the second processing step. Together, these observations are all consistent with a thermodynamic equilibrium interpretation, where the initial large deviation occurs as the system moves from the bulk nominal composition, located in a multi-phase field, to a multi-phase assemblage with components on phase boundaries. Then the subsequent small deviations of the $(Mn,Fe)_2(P,Si)$ phase composition after the second step are caused by the additional increases in carbide content, as the bulk nominal composition moves continually in a 5-D Mn–Fe–P–Si–C space and new phase equilibria are established.

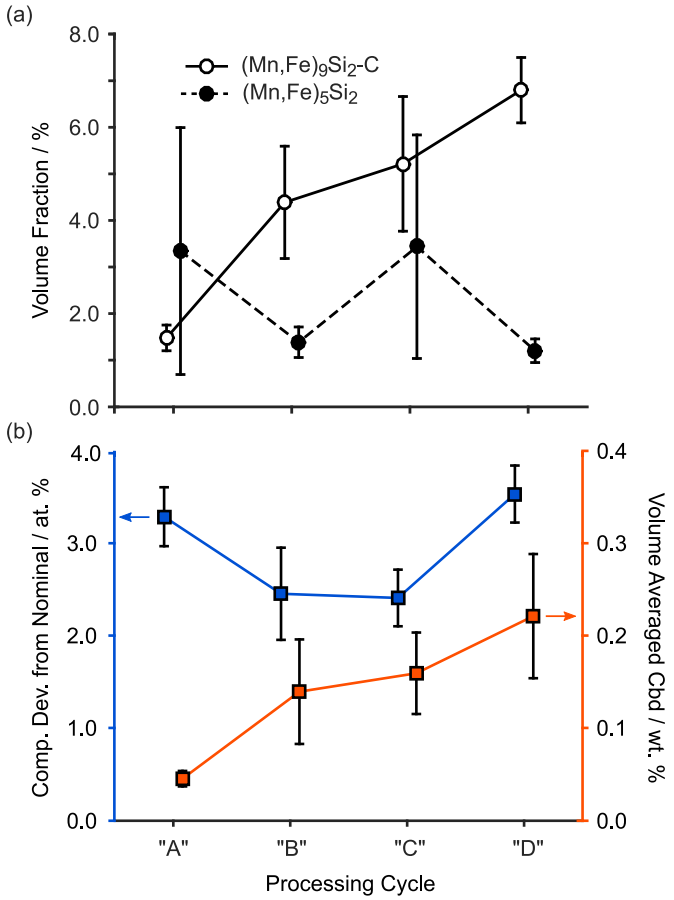

Fig. 5. Effect of repeated "A"-"D" processing cycles on (a) volume fractions of minority P-depleted impurity phases and (b) volume averaged C content and quaternary phase composition deviation, taken as the L_2 norm of the deviation vector (ΔMn, ΔFe, ΔP, ΔSi). Means and standard deviations calculated from set of 5 BSE images for each "A"-"D" cycle.

4.2. Phase coexistence relationships

In order to further provide evidence for this thermodynamic mechanism by which carbon impurities affect the composition of the emergent $(Mn,Fe)_2(P,Si)$ phase, as well as study the detailed equilibria between the phases present, we have re-plotted the measured compositions of all the phases as tie lines within a quaternary phase diagram. To assist with visualization, the C dimension has been neglected, leaving a Mn–Fe–P–Si Gibbs tetrahedron which has then been projected onto each of its faces, yielding four coupled pseudo-ternary Gibbs triangles (Fig. 6). Although for clarity we have not also shown all of the bulk nominal compositions, a "typical" bulk composition of ($x = 1.239$, $y = 0.559$) is shown (red diamond), which is clearly bounded by the tie lines defined by the observed phases in all of the projections, as required in the proposed multi-phase field interpretation.

The projections also enable more direct visualization of the pairwise phase coexistences in the system. To see this, note that phase clouds that overlap each other in the X-Y-Z pseudo-ternary Gibbs triangle necessarily differ only in the missing component W, since the tie line between the phases is evidently perpendicular to the X-Y-Z plane. For example, taking X = Mn, Y = Fe, Z = Si, W = P=, in the lower-left pseudo-ternary projection, it is immediately clear that the overlapping $(Mn,Fe)_2(P,Si)$ and $(Mn,Fe)_9Si_2$–C phases differ only in their P content (Fig. 6, dashed red circle). In other words, although there is certainly partitioning of P into the $(Mn,Fe)_2(P,Si)$ phase and out of the $(Mn,Fe)_9Si_2$–C phase as the system moves from the multi-phase field to its phase boundaries, there is no additional partitioning of Mn, Fe, or Si within these phases. Similarly, $(Mn,Fe)_5Si_2$ and $(Mn,Fe)_9Si_2$–C form together through a partition of only Mn, and $(Mn,Fe)_3Si_2$ and $(Mn,Fe)_5Si_2$ form together through a partition of only Fe. This suggests that the total phase equilibria between all phases in the 4-D composition space may be decomposed as relatively simple one-component pairwise equilibria, which may be a more useful way to visualize and explore equilibria in the complicated 4-D space. In any case, the

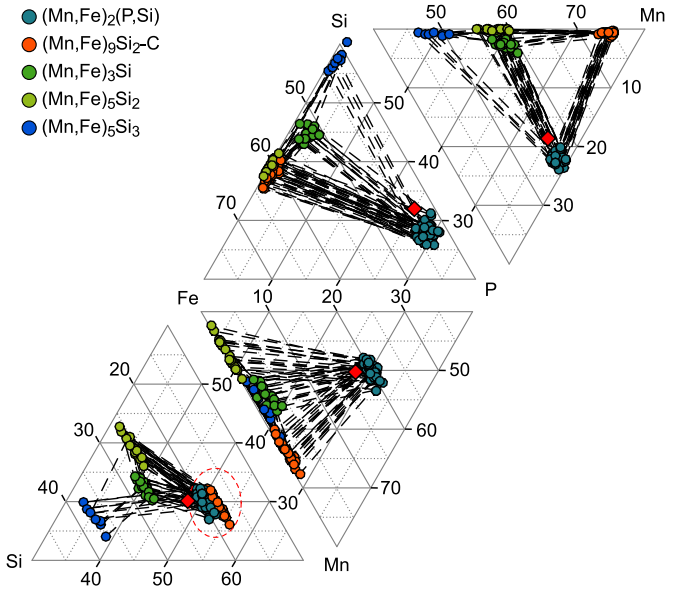

Fig. 6. Observed phase coexistence relationships in Mn–Fe–P–Si system, as projected onto each face of Gibbs tetrahedron. Red diamond marks "typical" bulk nominal composition, and red dashed circle marks overlapping $(Mn,Fe)_2(P,Si)$ and $(Mn,Fe)_9Si_2$ phases in Mn–Fe–Si pseudo-ternary projection, as discussed in section 4.2. (For interpretation of the references to colour in this figure legend, the reader is referred to the Web version of this article.)

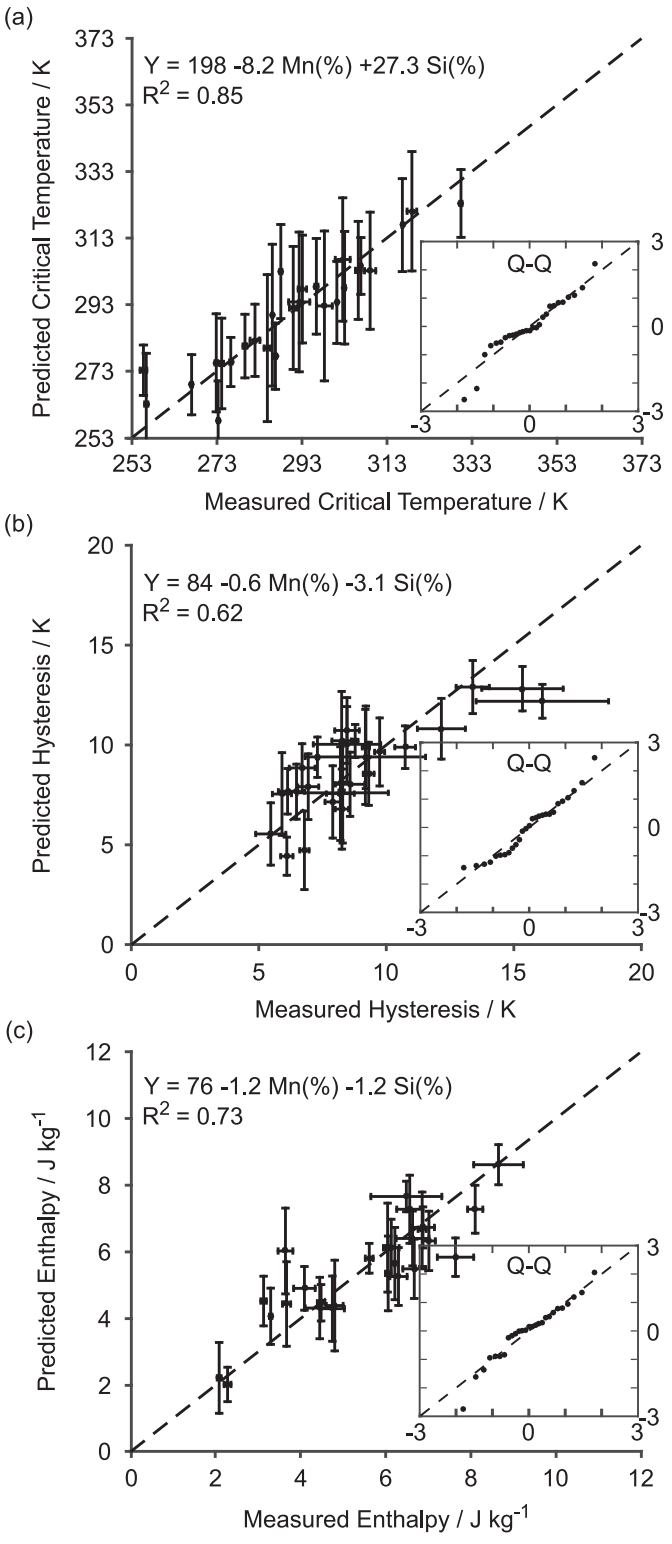

Fig. 7. Multilinear regressions for dependence of transformation (a) critical temperatures, (b) hystereses, (c) enthalpies measured from 10 K min^{-1} DSC ramps on Mn and Si content in $(Mn,Fe)_2(P,Si)$ phase. Goodness-of-fit (GOF) indicated by adjusted coefficients of determination R^2 and semi-linear normal quantile-quantile (Q–Q) plots (insets) and GOF parameters (Table 3).

Table 3
Summary of fitting parameters and goodness-of-fit parameters for multilinear regressions $\widehat{Y} = b_0 + b_1(\mathrm{Mn}) + b_2(\mathrm{Si})$. Adjusted coefficients of determination R^2 and target-residual correlations $\rho(Y, Y-\widehat{Y})$ are unitless; standard error of the regression S has same units U as data Y; slopes b_i and standard errors $\mathrm{se}(b_i)$ have units of either U or U/at. %.

Predicted Var.	$\boldsymbol{b_0 \pm \mathrm{se}(b_0)}$	$\boldsymbol{b_1 \pm \mathrm{se}(b_1)}$	$\boldsymbol{b_2 \pm \mathrm{se}(b_2)}$	$\boldsymbol{R^2}$	$\boldsymbol{\rho(Y,\ Y-\widehat{Y})}$	$\boldsymbol{S}$
Critical Temperature	198 ± 66	−8.2 ± 1.5	27.3 ± 2.3	0.85	0.37	6.7
Therm. Hysteresis	84 ± 15	−0.6 ± 0.4	−3.1 ± 0.5	0.62	0.60	1.6
Trans. Enthalpy	76 ± 8	−1.2 ± 0.2	−1.2 ± 0.3	0.73	0.50	0.9

analysis conclusively demonstrates deviations in the composition of the transforming phase from bulk nominal are caused by partitioning due to the presence of other equilibrium phases, with this partitioning also being coupled to the total carbon content of the system.

4.3. Effect of quaternary phase composition on transformation properties

Having measured the composition of all observed phases and established a carbon-mediated phase stability mechanism for modulating the composition of the $(Mn,Fe)_2(P,Si)$ phase of interest, we may now determine the effect of this mechanism on that phase's effective transformation properties. It is already well-known that transformation properties in $(Mn,Fe)_2(P,Si)$ alloys are strongly composition-dependent. However, it may be somewhat under-appreciated that these properties depend meaningfully on the composition of the $(Mn,Fe)_2(P,Si)$ phase alone, and due to the carbon-mediated phase segregation mechanism, this can potentially deviate substantially from the bulk nominal composition.

In order to investigate this fundamental composition dependence, first-order transformation critical temperatures, hystereses, and enthalpies have all been computed from DSC traces taken at 10 K min^{-1} for each "A" and "B" processed $(Mn_xFe_{2-x})(P_{1-y}Si_y)$ alloy throughout the bulk nominal $(1.18 \leq x \leq 1.28)$ and $(0.53 \leq y \leq 0.61)$ composition space. Each first-order transformation property has been fit against the measured $(Mn,Fe)_2(P,Si)$ phase composition with a 2-D linear regression of the form

$$\widehat{Y} = b_0 + b_1 X_1 + b_2 X_2 \tag{1}$$

with $\widehat{Y}$ the transformation properties predicted by the model, and X_1 and X_2 the independent Mn and Si contents of the $(Mn,Fe)_2(P,Si)$ phase measured from WDS.

The corresponding multilinear regressions (Fig. 7) show fairly good agreement between the model and predictions, with reasonably high R^2 values and generally linear normal quantile-quantile (Q-Q) plots implying a highly linear mapping from the $(Mn,Fe)_2(P,Si)$ phase composition onto the transformation properties, as expected. The Goodness-of-fit (GOF) for the models can be further compared (Table 3) by referencing the relative error in the fitting parameters $\mathrm{se}(b_i)/b_i$, the adjusted coefficient of determination R^2, the data-residuals correlation $\rho(Y, Y-\widehat{Y})$, and the standard error of regression S relative to the overall range of the data. This comparison suggests the critical temperature and enthalpy maps are relatively well-fit, with relative errors in b_i of 10–25%; $R^2 > \rho(Y, Y-\widehat{Y})$, implying the model predictions are more highly correlated with the data than the model errors; and S only about 12–15% of the total data range, implying precision in the model predictions of 12–15%. The GOF for the composition-hysteresis mapping is worse, with larger 15–65% relative error in fitting parameters, $R^2 \sim \rho(Y, Y-\widehat{Y})$, and S on the order of 15%; the Q-Q plot also deviates somewhat more from straight-line behavior.

Overall, there is reasonably good confidence in the regression coefficients for the critical temperatures and enthalpies, with critical temperatures increasing by about 27 K/at. % Si and decreasing by about −8 K/at. % Mn, and enthalpies decreasing by about −1 (J/g)/at. % Mn or Si. The rate of increase of critical temperature with Si is especially large, and the relatively large deviation of $(Mn,Fe)_2(P,Si)$ phase Si content from bulk nominal of −3 to −4 at. % (Fig. 3) implies the transformation critical temperatures may deviate from desired design values by as much as 100 K. Similarly, transformation hysteresis decreases by about −1 K/at. % Mn and −3 K/at. % Si, with Si again having a larger effect, although the worse GOF should be kept in mind. The critical temperature regression slopes are in good agreement with the −7 K/at. % Mn decrease for reported in $(Mn_xFe_{2-x})(P_{0.4}Si_{0.6})$ [44], as well as with regression fits we have extracted for similarly-prepared samples from plots in Ref. [13] (Table 4). The hysteresis regression slopes are in slightly worse agreement with [13] but are of the same sign and similar magnitude, likely due to slight differences in processing. Although the regression slopes reported here and in the literature are in good agreement, the constant offsets b_0 disagree substantially, especially for the hysteresis regression. Such disagreement could result from deviations in the nominal and actual $(Mn,Fe)_2(P,Si)$ composition similar to those observed here, and we note that sometimes very high contrast BSE settings are needed to distinguish the impurity phases, especially $(Mn,Fe)_5Si_2$ from the $(Mn,Fe)_2(P,Si)$ phase of interest.

Table 4
Computed linear regression fits to the composition maps of critical temperature and hysteresis reported in Ref. [13].

Predicted Var.	$\boldsymbol{b_0}$	$\boldsymbol{b_1}$	$\boldsymbol{b_2}$
Critical Temperature	183	−7.57	23.7
Therm. Hysteresis	190	−2.65	−4.54

5. Conclusion

Through comprehensive characterization of the compositions of main and impurity phases observed throughout the $(Mn_xFe_{2-x})(P_{1-y}Si_y)$ alloy system, we have shown that observed microstructures and compositional deviations of 1–4 at. % in the magnetocaloric $(Mn,Fe)_2(P,Si)$ phase from bulk nominal are consistent with a thermodynamic interpretation, with the system moving from an initial multi-phase field towards the phase boundaries. Additional annealing steps fail to either eliminate the impurity phases or the initial large composition deviation, instead tending to stabilize one of the impurity phases, as carbon impurities aggregate into P-poor carbides, and move the system towards slightly perturbed equilibria in a 5-D Mn–Fe–P–Si–C composition space. Whether the initial placement of the system within a multi-phase field is also caused by carbon or is inherent to equilibrium in the 4-D Mn–Fe–P–Si space is as yet an open question, but either way, the analysis shows that small carbon impurities have outsized effects on transformation properties, and studies using multiple homogenizing processing steps should carefully consider the trade-offs between homogenization and unintentional carbide

formation. Finally, compositional maps have been developed to quantify the effect of these carbon-mediated composition deviations on the caloric transformation properties, showing that typical deviations of +1.5 at. % Mn and −3 at. % Si cause transformation hysteresis, enthalpy, and critical temperature deviations of +8 K, +3 J/g, and −95 K, respectively. Designing these transformation properties within narrow tolerances is critical for future development of these alloys for practical magnetic refrigeration applications, and so continuing work to investigate the phase fields, especially in the carbon-free alloy system, is crucial.

Funding

This work was supported by the U.S. National Science Foundation [grant numbers CMMI-1636105, DGE-1252521, EEC-1005178, and EEC-1461202].

Declaration of competing interest

The authors declare that they have no known competing financial interests or personal relationships that could have appeared to influence the work reported in this paper.

CRediT authorship contribution statement

T.D. Brown: Conceptualization, Methodology, Investigation, Visualization, Writing - original draft. **D. Galvan:** Resources, Investigation. **J. van Buskirk:** Investigation, Formal analysis. **A. Mott:** Investigation, Formal analysis, Writing - review & editing. **P.J. Shamberger:** Conceptualization, Supervision, Writing - review & editing.

Acknowledgments

The authors acknowledge H. N. Jones for her role in helping to determine the carbon content of the $(Mn,Fe)_9Si$ impurity phases.

Appendix A. Supplementary data

Supplementary data to this article can be found online at https://doi.org/10.1016/j.jallcom.2020.154532.

References

[1] A. Fujita, S. Fujieda, Y. Hasegawa, K. Fukamichi, Itinerant-electron metamagnetic transition and large magnetocaloric effects in $\mathrm{La}({\mathrm{Fe}}_{x}{\mathrm{Si}}_{1\ensuremath{-}x}{)}_{13}$ compounds and their hydrides, Phys. Rev. B 67 (2003), 104416.
[2] F.X. Hu, B.G. Shen, J.R. Sun, Z.H. Cheng, G.H. Rao, X.X. Zhang, Influence of negative lattice expansion and metamagnetic transition on magnetic entropy change in the compound LaFe11.4Si1.6, Appl. Phys. Lett. 78 (2001) 3675–3677.
[3] J. Liu, T. Gottschall, K.P. Skokov, J.D. Moore, O. Gutfleisch, Giant magnetocaloric effect driven by structural transitions, Nat. Mater. 11 (2012) 620–626.
[4] N.H. Dung, L. Zhang, Z.Q. Ou, E. Bruck, Magnetoelastic coupling and magnetocaloric effect in hexagonal Mn-Fe-P-Si compounds, Scripta Mater. 67 (2012) 975–978.
[5] K.A. Gschneidner, V.K. Pecharsky, Thirty years of near room temperature magnetic cooling: where we are today and future prospects, Int. J. Refrig. 31 (2008) 945–961.
[6] E. Brück, Developments in magnetocaloric refrigeration, J. Phys. Appl. Phys. 38 (2005) R381–R391.
[7] O. Tegus, E. Bruck, K.H.J. Buschow, F.R. de Boer, Transition-metal-based magnetic refrigerants for room-temperature applications, Nature 415 (2002) 150–152.
[8] A. Post, C. Knight, E. Kisi, Thermomagnetic energy harvesting with first order phase change materials, J. Appl. Phys. 114 (2013).
[9] A. Waske, D. Dzekan, K. Sellschopp, D. Berger, A. Stork, K. Nielsch, S. Fahler, Energy harvesting near room temperature using a thermomagnetic generator with a pretzel-like magnetic flux topology, Nat Energy 4 (2019) 68–74.
[10] S. Jeong, AMR (Active Magnetic Regenerative) refrigeration for low temperature, Cryogenics 62 (2014) 193–201.
[11] J.C. Debnath, R. Zeng, J.H. Kim, P. Shamba, S.X. Dou, Reduction of hysteresis loss in LaFe11.7Si1.3H x hydrides with significant magnetocaloric effects, Appl. Phys. A 106 (2011) 245–250.
[12] M. Khan, N. Ali, S. Stadler, Inverse magnetocaloric effect in ferromagnetic Ni50Mn37+xSb13−x Heusler alloys, J. Appl. Phys. 101 (2007).
[13] N.H. Dung, Z.Q. Ou, L. Caron, L. Zhang, D.T.C. Thanh, G.A. de Wijs, R.A. de Groot, K.H.J. Buschow, E. Brück, Mixed magnetism for refrigeration and energy conversion, Adv. Energy Mater. 1 (2011) 1215–1219.
[14] Y.F. Chen, F. Wang, B.G. Shen, J.R. Sun, G.J. Wang, F.X. Hu, Z.H. Cheng, T. Zhu, Effects of carbon on magnetic properties and magnetic entropy change of the LaFe11.5Si1.5 compound, J. Appl. Phys. 93 (2003) 6981–6983.
[15] S. Fu, Y. Long, W. Sun, X.P. Yi, Y.Q. Chang, R.C. Ye, K. Yang, Influence of silicon and carbon elements on formation of 1:13 phase and microstructure in LaFe13-ySiy compounds, J. Rare Earths 30 (2012) 1225–1227.
[16] P. Gebara, P. Pawlik, M. Hasiak, Alteration of negative lattice expansion of the La(Fe,Si)(13)-type phase in LaFe11.14-xCo0.66NixSi1.2 alloys, J. Magn. Magn Mater. 422 (2017) 61–65.
[17] H. Zhang, Y. Long, Q. Cao, Y. Mudryk, M. Zou, K.A. Gschneidner, V.K. Pecharsky, Microstructure and magnetocaloric effect in cast LaFe11.5Si1.5Bx (x=0.5, 1.0), J. Magn. Magn Mater. 322 (2010) 1710–1714.
[18] S.Y. Yang, Y. Su, C.P. Wang, J.H. Zhu, X.J. Liu, Microstructure, martensitic transformation and shape memory effect of Ni38Co12Mn41In9 alloy, Mater. Lett. 108 (2013) 215–218.
[19] S.Y. Yang, C.P. Wang, Z. Shi, J.M. Wang, J.B. Zhang, Y.X. Huang, X.J. Liu, Microstructure, martensitic transformation, mechanical and shape memory properties of Ni-Co-Mn-In high-temperature shape memory alloys under different heat treatments, Mater. Sci. Eng. A-Struct. Mater. Prop. Microstruct. Process. 655 (2016) 204–211.
[20] Y. Feng, J.H. Sui, Z.Y. Gao, G.F. Dong, W. Cai, Microstructure, phase transitions and mechanical properties of Ni50Mn34In16-yCoy alloys, J. Alloys Compd. 476 (2009) 935–939.
[21] F. Chen, W.L. Liu, Y.G. Shi, P. Mullner, Influence of annealing on martensitic transformation and magnetic entropy change in Ni37.7Co12.7Mn40.8Sn8.8 magnetic shape memory alloy ribbon, J. Magn. Magn Mater. 377 (2015) 137–141.
[22] J. Liu, T.G. Woodcock, N. Scheerbaum, O. Gutfleisch, Influence of annealing on magnetic field-induced structural transformation and magnetocaloric effect in Ni-Mn-In-Co ribbons, Acta Mater. 57 (2009) 4911–4920.
[23] X.L. Hou, Y. Xue, C.Y. Liu, H. Xu, N. Han, C.W. Ma, M.H. Phan, Nucleation mechanism of nano-sized NaZn13-type and alpha-(Fe,Si) phases in La-Fe-Si alloys during rapid solidification, Nanoscale Res Lett 10 (2015) 1–6.
[24] X.D. Liu, X.B. Liu, Z. Altounian, G.H. Tu, Microstructures of (Fe0.88Co0.12)(82) La7Si11 prepared by arc-melting/melt spinning and subsequent annealing, Appl Phys a-Mater 82 (2006) 339–343.
[25] H. Zhang, B. Bao, P.J. Shi, B. Fu, Y. Long, Y.Q. Chang, F.R. Wan, Phase formation with NaZn13 structure in metamagnetic La(Fe1-xCox)(11.9)Si-1.1 compounds, J. Rare Earths 26 (2008) 727–730.
[26] S. Fu, Y. Long, C.L. Wang, M. Zhang, O. Soumei, F.X. Hu, formation of 1:13 phase in La(Fe,Si)(13)-Based compounds by diffusion of LaFe,Si/alpha-Fe(Si) couple, IEEE Trans. Magn. 48 (2012) 3757–3759.
[27] L. Yang, Z.N. Zhou, J.R. Qian, X. Ge, J. Li, Q.D. Hu, J.G. Li, Peritectic solidification path of the La(Fe,Si)(13) phase in dual-phase directionally solidified La-Fe-Si magnetocaloric alloys, Metall. Mater. Trans. 48a (2017) 4229–4236.
[28] G. Potnis, M. Krautz, A. Waske, J. Das, J. Eckert, Assessing two rapid quenching techniques for the production of La-Fe-Si magnetocaloric alloys in reduced annealing time, Mater. Des. process. Commun. 1 (2019) 1–9.
[29] J. Lyubina, O. Gutfleisch, M.D. Kuz'min, M. Richter, La(Fe,Si)(13)-based magnetic refrigerants obtained by novel processing routes (vol 320, pg 2252, 2008), J. Magn. Magn Mater. 321 (2009) 3571–3577.
[30] M. Phejar, V. Paul-Boncour, L. Bessais, Structural and magnetic properties of magnetocaloric LaFe13-xSix compounds synthesized by high energy ball-milling, Intermetallics 18 (2010) 2301–2307.
[31] X.B. Liu, Z. Altounian, G.H. Tu, The structure and large magnetocaloric effect in rapidly quenched LaFe11.4Si1.6 compound, J Phys-Condens Mat 16 (2004) 8043–8051.
[32] X.B. Liu, X.D. Liu, Z. Altounian, G.H. Tu, Phase formation and structure in rapidly quenched La(Fe0.88Co0.12)(13-x)Si-x alloys, J. Alloys Compd. 397 (2005) 120–125.
[33] A.M. Perez-Sierra, J. Pons, R. Santamarta, P. Vermaut, P. Ochin, Solidification process and effect of thermal treatments on Ni-Co-Mn-Sn metamagnetic shape memory alloys, Acta Mater. 93 (2015) 164–174.
[34] J.K. Yu, H.W. Li, Q.J. Zhai, J.X. Fu, Z.P. Luo, H.X. Zheng, Crystal structure and formation mechanism of the secondary phase in Heusler Ni-Mn-Sn-Co materials, Adv. Manuf. 2 (2014) 353–357.
[35] X.F. Miao, L. Caron, P. Roy, N.H. Dung, L. Zhang, W.A. Kockelmann, R.A. de Groot, N.H. van Dijk, E. Bruck, Tuning the phase transition in transition-metal-based magnetocaloric compounds, Phys. Rev. B 89 (2014) 6.
[36] N.T. Trung, Z.Q. Ou, T.J. Gortenmulder, O. Tegus, K.H.J. Buschow, E. Brück, Tunable thermal hysteresis in MnFe(P,Ge) compounds, Appl. Phys. Lett. 94 (2009).
[37] A. He, V. Svitlyk, Y. Mozharivskyj, Synthetic approach for (Mn,Fe)(2)(Si,P) magnetocaloric materials: purity, structural, magnetic, and magnetocaloric properties, Inorg. Chem. 56 (2017) 2827–2833.
[38] V. Hoglin, M. Hudl, L. Caron, P. Beran, M.H. Solby, P. Nordblad, Y. Andersson,

M. Sahlberg, Detailed study of the magnetic ordering in FeMnP0.75Si0.25, J. Solid State Chem. 221 (2015) 240–246.
[39] V. Hoglin, J. Cedervall, M.S. Andersson, T. Sarkar, M. Hudl, P. Nordblad, Y. Andersson, M. Sahlberg, Phase diagram, structures and magnetism of the FeMnP1-xSix-system, RSC Adv. 5 (2015) 8278–8284.
[40] Z.G. Zheng, Z.R. Zhu, H.Y. Yu, D.C. Zeng, Y.H. Li, A. He, Y. Mozharivskyj, Large magnetic entropy change and magnetic phase transitions in rapidly quenched bulk Mn-Fe-P-Si alloys, J. Alloys Compd. 725 (2017) 1069–1076.
[41] J.H. Grebenkemper, J.D. Bocarsly, E.E. Levin, G. Seward, C. Heikes, C. Brown, S. Misra, F. Seeler, K. Schierle-Arndt, S.D. Wilson, R. Seshadri, Rapid microwave preparation and composition tuning of the high-performance magnetocalorics (Mn,Fe)(2)(P,Si), ACS Appl. Mater. Interfaces 10 (2018) 7208–7213.
[42] K. Katagiri, K. Nakamura, H. Wada, Magnetocaloric properties and magnetic refrigerant capacity of MnFeP1-xSix, J. Alloys Compd. 553 (2013) 286–290.
[43] Y.X. Geng, O. Tegus, L.G. Bi, Magnetocaloric effects in Mn1.35Fe0.65P1-xSix compounds, Chin. Phys. B 21 (2012).
[44] Y.X. Geng, Z.J. Zhang, O. Tegus, C. Dong, Y.X. Wang, Microstructure, magnetic and magnetocaloric properties of Fe2-xMnxP0.4Si0.6 alloys, Sci China Mater 59 (2016) 1062–1068.
[45] Z.G. Zheng, W.H. Wang, Q. Zhou, L. Lei, Y. Hong, D.C. Zeng, Y. Mozharivskyj, Microstructure and magnetocaloric effects of Mn1.2Fe0.8P0.6Si0.4B0.05 alloys prepared by ball milling and spinning methods, J. Magn. Magn Mater. 477 (2019) 203–208.
[46] F. Guillou, H. Yibole, N.H. van Dijk, E. Bruck, Effect of boron substitution on the ferromagnetic transition of MnFe0.95P2/3Si1/3, J. Alloys Compd. 632 (2015) 717–722.
[47] J.W. Lai, Z.G. Zheng, B.W. Huang, H.Y. Yu, Z.G. Qiu, Y.L. Mao, S. Zhang, F.M. Xiao, D.C. Zeng, K. Goubitz, E. Bruck, Microstructure formation and magnetocaloric effect of the Fe2P-type phase in (Mn,Fe)(2)(P, Si, B) alloys, J. Alloys Compd. 735 (2018) 2567–2573.
[48] M. Fries, L. Pfeuffer, E. Bruder, T. Gottschall, S. Ener, L.V.S. Diop, T. Grob, K.P. Skokov, O. Gutfleisch, Microstructural and magnetic properties of Mn-Fe-P-Si (Fe-2 P-type) magnetocaloric compounds, Acta Mater. 132 (2017) 222–229.
[49] Q. Zhou, Z.G. Zheng, W.H. Wang, L. Lei, A. He, D.C. Zeng, Carbon doping in the Mn1.15Fe0.80P0.50Si0.50 materials: structure, phase transition and magnetocaloric properties, Intermetallics 106 (2019) 94–99.
[50] N. Chakraborti, H.L. Lukas, Calculation and optimization of the Mn-Si phase-diagram, Calphad 13 (1989) 293–300.
[51] P.Y. Chevalier, E. Fischer, A. Rivet, A thermodynamic evaluation of the Mn-Si system, Calphad 19 (1995) 57–68.
[52] A. Shukla, Y.B. Kang, A.D. Pelton, Thermodynamic assessment of the Si-Zn, Mn-Si, Mg-Si-Zn and Mg-Mn-Si systems, Calphad 32 (2008) 470–477.
[53] M.K. Paek, J.J. Pak, Y.B. Kang, Phase equilibria and thermodynamics of Mn-C, Mn-Si, Si-C binary systems and Mn-Si-C ternary system by critical evaluation, combined with experiment and thermodynamic modeling, Calphad 46 (2014) 92–102.
[54] P. Spinat, J.P. Senateur, P. Herpin, R. Fruchart, Characterization of 2 Isotype Phases Mn8si2c and Fe8si2c, Cr Acad Sci C Chim 274 (1972) 1159–&.
[55] P. Spinat, P. Herpin, Neutron-diffraction studies of Mn-5sic phase and solid-solutions (Mn-1-Xmo-X)5 sic, (Mn-1-Xfe-X)5 sic - structural and magnetic-properties, B Soc Fr Mineral Cr 99 (1976) 13–20.